Received: 26 March 2022 | Revised: 26 May 2022 | Accepted: 24 July 2022

DOI: 10.1002/eqe.3724

RESEARCH ARTICLE

WILEY

Experimental and analytical study of Friction Connection for seismic retrofit with Cross-Laminated Timber (CLT) panels

Francesco Boggian[1,2] | **Angelo Aloisio**[1,3] | **Roberto Tomasi**[1]

[1]Faculty of Science and Technology, Norwegian University of Life Sciences, Ås, Norway

[2]Department of Civil, Environmental and Mechanic Engineering, University of Trento, Trento, Italy

[3]Department of Civil Engineering, University of L'Aquila, L'Aquila, Italy

Correspondence
Francesco Boggian, Faculty of Science and Technology, Norwegian University of Life Sciences, Ås, Norway.
Email: francesco.boggian@nmbu.no

Funding information
Horizon 2020, Grant/Award Number: 893135; European Commission

Abstract

Within the European project e-SAFE (Energy and Seismic AFfordable rEnovation solutions), this paper presents the experimental tests and modeling attempts for a class of Asymmetric Friction Connections (AFCs) tested in the laboratories of the Norwegian University of Life Sciences. The AFCs are part of the seismic retrofitting solution, called e-CLT, based on installing Cross-Laminated Timber (CLT) panels in reinforced concrete structures using friction connections. The authors carried out experimental tests on AFCs fixed with screws to a CLT panel to observe the contribution of timber to the total dissipation performance. The investigation is based on 20 cyclic test data with two different setups. The main one includes a CLT panel and screw connection, while the second one isolates the friction behaviour to evaluate the influence of the screw connection. A modified LuGre hysteresis model for friction is developed to simulate the experimental cyclic response of the tested specimen. The model possesses a direct physical meaning, and it explicitly depends on the slip force and the pre-slip stiffness. The optimized model is used to assess the performance of the AFC by varying the pre-slip stiffness and the slip force.

KEYWORDS
CLT, friction connection, seismic, energy dissipation, renovation

1 | INTRODUCTION

There are three primary dissipation devices for seismic retrofitting purposes: the Active, Semi-Active, and Passive devices.[1–6] The most used passive dampers are probably the hysteretic devices, generally used for base isolation.[7,8] However, among hysteretic devices, friction dampers have been gaining more attention in the last few years. These dampers dissipate seismic energy by mechanical damping through sliding friction with the primary "braking rather than breaking" principle.[9] There is a wide range of applications of friction dampers, from civil to mechanical and avionic engineering.[10,11] However, there are still a few attempts in using friction dampers for seismic retrofitting of civil structures. Pall et al.,[9] was the first to add friction devices as additional damping sources in civil structures. The Limited Slip Bolt (LSB), evolved to the Pall Frictional Damper (PFD), exhibited stable, almost rectangular hysteresis cycles.[12,13] PFD are conceived for X- and K-bracings. Its worldwide success has confirmed the merits of the PFD. Multiple applications and research papers are proving the value and efficiency of the PFD.[14–17] The main drawbacks of PFD are the relatively low capacity (less than 10 kips), the need for high precision work for its manufacture and specialized training for the installation process.[18,19]

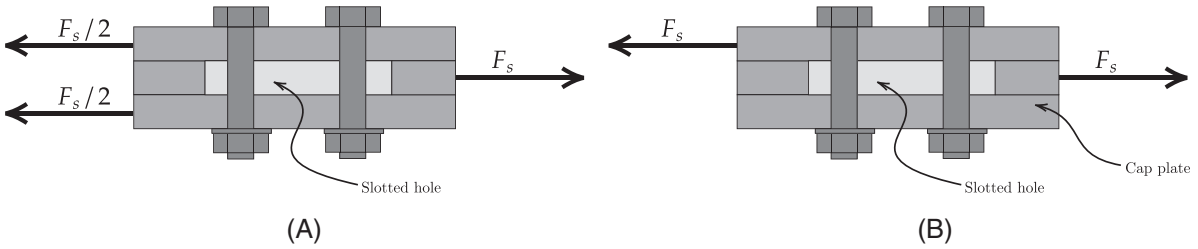

FIGURE 1 (A) Symmetric and (B) Asymmetric Friction connections

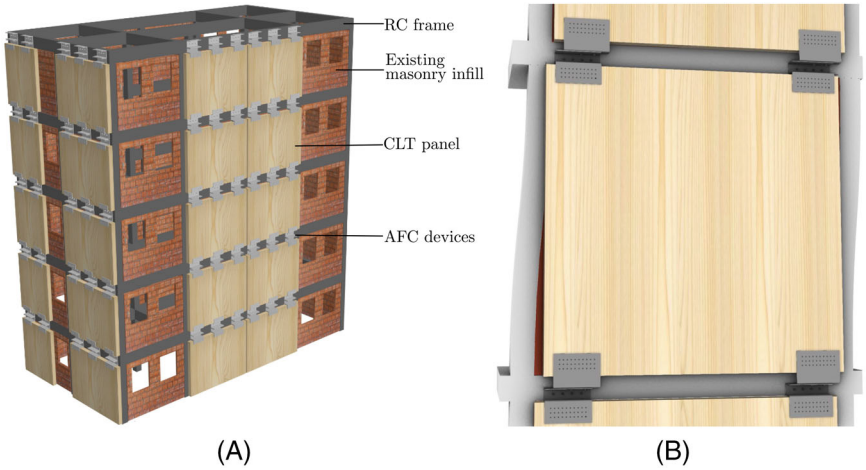

FIGURE 2 e-CLT seismic retrofit system, modified from[40]

In 1989 Fitzgerald et al.[20] devised a friction connection called Slotted Bolted Connection (SBC), characterized by a more straightforward design than the PFD. The proposed SBC worked by sliding channel bracing plate over a gusset plate interconnected by high strength bolts with washers (Belleville spring) for adjusting the bolt tension. There are two main classes of SBC: the Symmetric and Asymmetric friction connection (AFC),[21,22] see Figure 1. Both system are based on using three main plates clamped together with pre tensioned bolts, with the central one presenting a slotted hole that allows for the sliding movement. Shim layers of different materials may be present in the two shear plane to improve friction stability. Symmetric Friction Connection (SFC) is a type of SBC where the loading condition is symmetric, so the sliding force is applied to the middle slotted plate and the reaction force is divided equally between the other two plates. Initially proposed by Clifton, AFC is another type of SBC.[23,24] In this case the loading condition is asymmetric: the sliding force is applied to the middle slotted plate but the reaction force is resisted only by one of the other two plates, so the other one act as a cap plate that is simply dragged by the rest of the system.[25]

There are already several experimental tests proving the successful hysteretic performance of the AFC. This paper discusses a possible application of AFC integrated with CLT panels for the seismic retrofitting of existing RC buildings.[26,27] AFCs are more commonly applied to steel buildings.[28] Friction devices coupled with other structural components are also known as hybrid systems. Among hybrid devices, the coupling between friction connections and timber embodies a significant innovation in structural engineering. Loo et al.[29] investigated the possibility of using SFC instead of hold-down for restraining timber shear walls against uplift, to cap the force transmitted to the wall, and reduce inelastic damage. The subsequent experimental campaigns by Ref.[30,31] established the effectiveness of SFC on reducing the degradation and pinching phenomena typical of timber connections. The following studies by Ref.[32] pointed to a displacement-based design method for multistory CLT buildings with friction connections. Following Ref.,[30,31] Fitzgerald et al.[33] studied the response of SFC connected to a CLT panel.[34] The combined use of CLT panels and AFC for the seismic retrofitting of RC structures has never been investigated so far.[35] In RC buildings with masonry infill, CLT panels can be used in addition, or substitution[36,37] of existing masonry infill. The main issue related to these interventions is executing an appropriate connection system between the CLT panel and the existing structure. The system suggested by the authors is called e-CLT, see Figure 2, and consists of CLT panel attached from the outside of the building while leaving the masonry infills unchanged, without discomfort for the people living inside the building.[38] The CLT panel is not inside the RC frame, as in the masonry infill, but in front of it. So its kinematics and deformation response does not interfere with the RC

frame during the seismic excitation. CLT panels are lightweight (around 470 kg/m^3), thus not significantly raising the mass of existing buildings. Non secondarily, CLT panels possess a high level of prefabrication and all the benefits of dry interventions. The major innovation of the e-CLT retrofitting intervention stands in the connection system between CLT and the existing building: an AFC. The AFC is constituted by a couple of steel profiles connected to the existing beam and the CLT panel, clamped together by preloaded bolts. One of the two profiles presents a slotted hole, which enables their mutual sliding. Single CLT panels are connected to the RC beams of the structure by at least two AFC. The possible critical point of this structural arrangement is related to the CLT panel uplift due to its significant in-plane stiffness. The uplift might cause a de-tensioning of the pre-loaded bolts. Therefore, particular attention must be paid to the stiffness of the connection, which should not adsorb the panel rotation. Parallelly, the e-CLT should be designed to withstand out-of-plane forces arising from the out-of-plane behaviour of the masonry infill. However, this aspect is outside the scope of the current research. The size of the CLT panels is related to that of the bays without openings where they are applied. The e-CLT technology can be combined with non-structural framed panels that may be applied to the walls with openings and are equipped with high-performing windows that replace the existing ones. Both panels integrate insulation materials to improve the energy efficiency of the building and finishing layer. The retrofit system also provides technological solutions to cover the AFC devices after the panels' installation, ensuring their inspection and maintenance.[39] Boggian et al.[40] focused on the shape optimization of the steel profiles and did not study the interaction with the timber component. The experimental activity was directed at isolating the friction behavior of the AFC, representing the innovative part of the system. However, the deformability and damage of the timber connection can potentially undermine the effectiveness of the friction connection. Therefore, the experimental investigation on the interaction between the AFC and the CLT panel should be understood. Given the above, the main novelties and objectives of this research are:

- Experimental tests of AFC connected to CLT specimens under cyclic loading;
- Comparison between experimental tests on AFC without connection to the CLT specimen to estimate the effect of the connection on the hysteretic response;
- Development of an analytical friction model, derived from the LuGre model, capable of mirroring the stabilization of the friction coefficient as dissipated energy grows; the model is a possible trade-off between model complexity and accuracy.
- Estimate the parameters of the proposed analytical model for each tested specimen using a global optimization algorithm;
- Evaluate the pre-slip stiffness effect and proposal a design formula to predict the lower bounds of the pre-slip stiffness to obtain a correct performance;
- Discussion on the performance of the tested assemblies under multiple repetitions of the same cyclic load protocol.

The paper has the following organization. The second section presents an introduction of the current experimental campaign by highlighting the differences to the previous one detailed in and details the experimental tests, while the third section deals with the results of the experimental tests. The fifth section deals with the analytical hysteresis modeling and the estimation of the parameters using a global optimization algorithm. The last section addresses the issue of pre-slip stiffness and stability of the dissipated energy. It also compares analytical formulations for predicting the stiffness of the screwed connection.

2 | MATERIALS AND METHODS

2.1 | Specimen

The specimen is called HYB (Hybrid), since its design originated from the results of the previous campaign:[40] STD offered the positive feature of the front mounting possibility, while ALT offered better mechanical performances due to the single bend L shape. HYB attempts to combine the best features of the two previous designs: front mounting and simple L shape, see Figures 3, 4. The reader is referred to Ref.[40] for the previous campaign, and to Ref.[41] for more details on the conceiving of this HYB design. The specimen is made of two 8 mm thick cold bent S355 steel profiles: the anchor profile is connected to the moving head of the press (the existing RC beam for the real world case), while the free profile is connected to the CLT panel. The two profiles are clamped together to form an AFC by adding an 8 mm steel cap plate and two 2 mm aluminum shim layers. The connection between the two profiles is ensured by two high strength M16 10.9 bolts,[42] that will slide in a 17

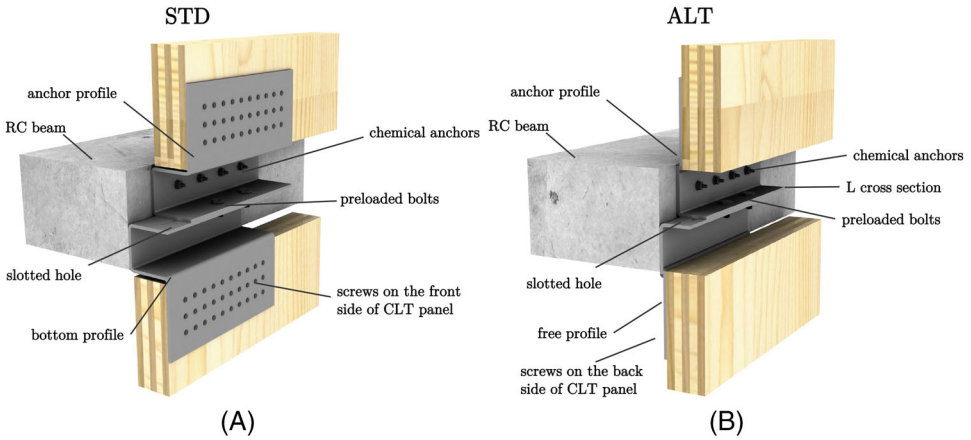

FIGURE 3 Specimen STD and ALT from previous experimental campaign[40]

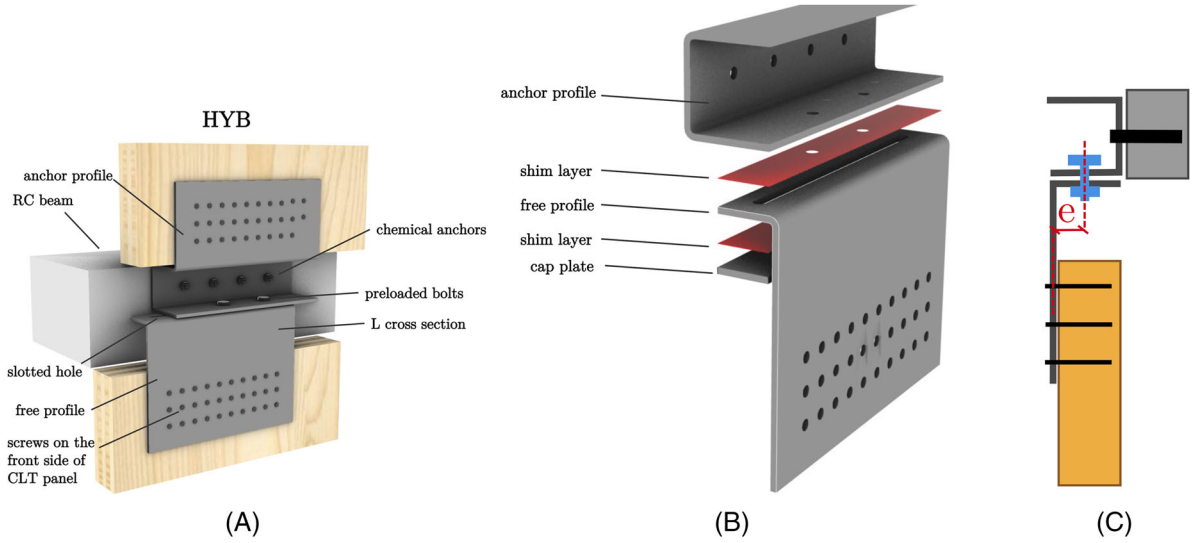

FIGURE 4 Specimen Hybrid (HYB) tested in the current experimental campaign: (A) parts of the system in a real building, (B) parts of the specimen used for testing, (C) eccentricity of the specimen

TABLE 1 Description of the specimens

Prototype	n.	e [mm]	Setup
HYB	3	52.5	with CLT
HYB_e	1	43.5	with CLT
HYB_s	1	52.5	no CLT

mm wide elongated hole. The elongated hole is 100 mm long plus some tolerance, and allows for relative sliding between the two profiles. The sliding length was chosen by considering the assumption that typical RC frame reach failure at an inter story drift of 3% of the story height, and a common height value for the type of building object of renovation is 3 m.

Three different types of specimen were tested, see Table 1. All had the same overall dimensions and shape, but presented small geometric variations. Specimens HYB (reference design, three samples) and HYB_e (one sample) differed in the eccentricity of the friction connection with respect to the screw connection, see Figure 4c: HYB had the elongated hole in the center of the specimen width, while in HYB_e the elongated hole was moved towards the CLT side, to see if this had an impact on the mechanical behavior. In both cases the free profile presented 33 holes for a screw connection to the CLT panel. The screws were 10 x 80 mm HBS Plate Evo from Rothoblaas.[43] Both these type of specimens were tested in the same setup, with a piece of CLT panel 100 mm thick, five layers and of dimensions 400 x 800 mm. The specimen

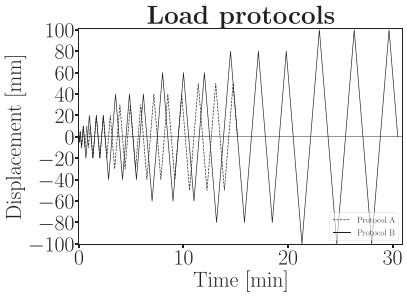

FIGURE 5 Load protocols: Protocol A: 1 ×5 mm+3×10-20-30-40-50 mm; 2 mm/s; Protocol B: 1 ×5-10 mm+3×20-40-60-80-100 mm; 2 mm/s

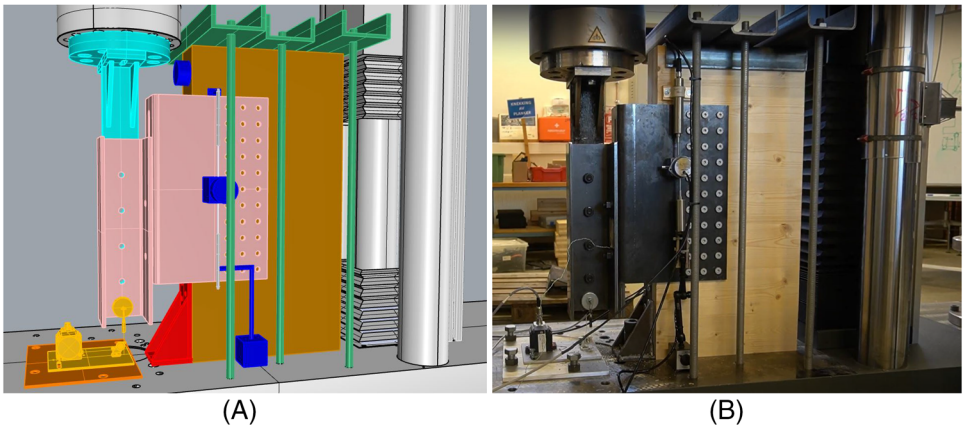

FIGURE 6 (A) Model of the setup, (B) picture of the setup. In both images the press is pushing down 100 mm

HYB_s (one sample), which had the same eccentricity as the HYB, was used on a different setup: a steel column was used as support for the free profile instead of a CLT panel, thus the hole pattern was different since bolts were used instead of screws. This specimen was made in order to have a direct comparison regarding the effect of the screw connection on the friction behavior of the system.

2.2 | Setup and load protocol

The tests were carried out in the timber laboratory of the Norwegian University of Life Sciences. The setup comprising the CLT panel can be seen in Figure 6, and was devised in order to simulate the sliding movement that would occur in a real building condition. The anchor profile, simplified to a C shape for testing purposes, was rigidly attached to a T shape element connected to the actuator of the press machine. The free profile was connected with screws to the CLT panel, which was held in place by a hold down and UPN profiles connected to base of the press with threaded rods. The hold down was custom made, with 10 mm thick steel plates, 22 10 x 80 mm screws for the timber and one M30 bolt at the base. The machine applied a vertical sliding movement, which would be equivalent to the horizontal movement of an RC beam in a real case building. The machine used for the experiments was electro mechanical, and recorded force measures with a load cell of 1200 kN capacity. Measures of displacement were recorded both by the press itself and by an additional wire sensor, attached to the anchor profile and aligned with the actuator. Additional sensors were placed to record the deformations of the screw connection and of the CLT panel. Two LDTs were placed on the free profile, taking vertical measures of the displacement at its center: one was fixed at the base of the press, and the other was fixed to the CLT, thus measuring the relative slip between the steel profile and timber. One inclinometer was placed on the free profile, and another one was placed on the narrow side of the CLT panel. The last LDT was placed on the opposite side at the base of the CLT panel, in order to check the sufficient stiffness of the hold down. A thermocouple measured the temperature on the friction connection. A drawing of the sensors layout and parts of the setup can be seen

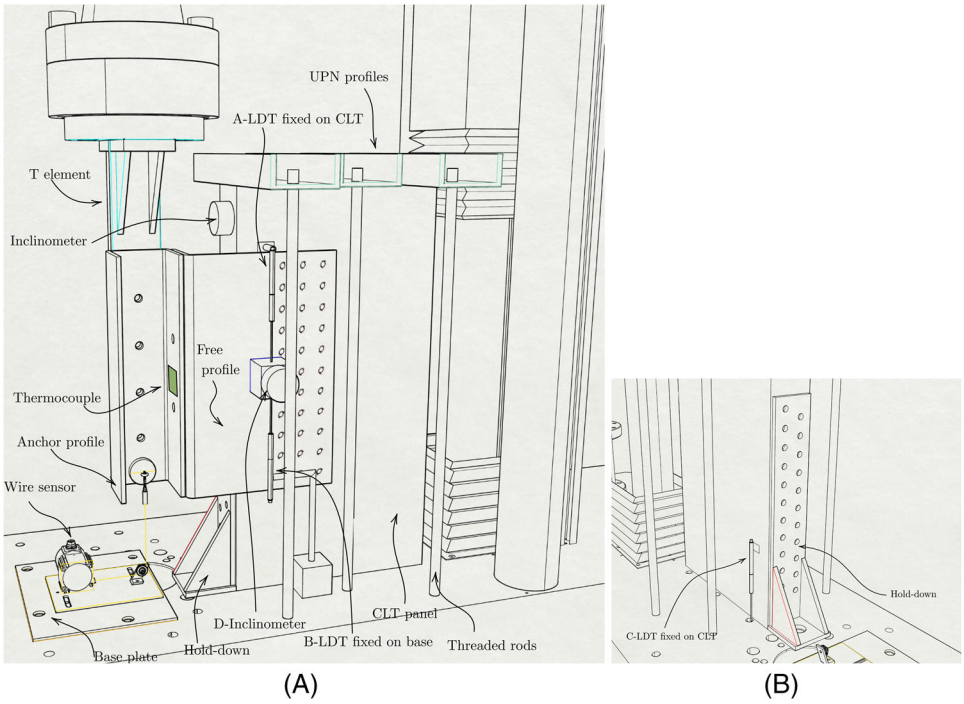

FIGURE 7 Parts of the Cross-Laminated Timber (CLT) setup. The letters associated with some of the sensors help the readability of the results in Figure 14

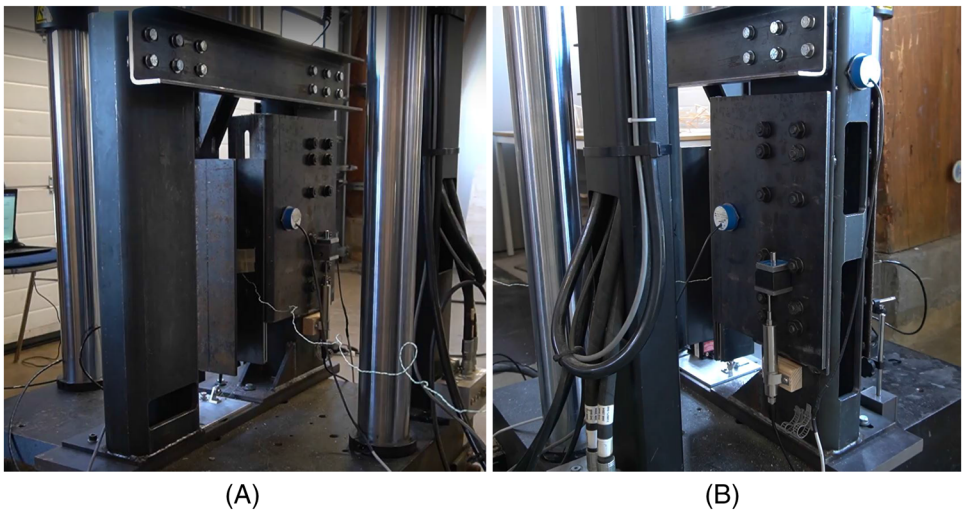

FIGURE 8 (A) Setup for HYB_s experiments, (B) detail of the free profile bolted to the steel column. In both images the press is pushing down 100 mm.

in Figure 7. The setup for the tests on the HYB_s specimen, which was tested without CLT panel to study the influence of the screw connection, was the same as the experiments presented in.[40] The fixed profile was connected to the press in the same way as the previous tests, while the free profile was rigidly connected to a steel column, part of a frame fixed at the base of the press, see Figure 8. The load protocol was applied in displacement control, with a constant speed of 2 mm/s. The protocol was cyclic, adapted from the prescriptions of EN15129,[44] which suggests incremental steps of displacement till reaching the ultimate displacement. In the case of friction connection the ultimate displacement was considered as the maximum sliding clearance of the elongated holes, which was 100 mm. The two protocols are visible in Figure 5.

TABLE 2 Overview of the tests

Test label	Specimen	Protocol	Setup	Preload [kN]
HYB-1.1	HYB-1	A	CLT	25.0
HYB-1.2		A	CLT	25.0
HYB-2.1	HYB-2	B	CLT	25.0
HYB-2.2		B	CLT	25.0
HYB-2.3		B	CLT	25.0
HYB-2.4		B	CLT	25.0
HYB-3.1	HYB-3	B	CLT	25.0
HYB-3.2		B	CLT	25.0
HYB-3.3		B	CLT	25.0
HYB-3.4		B	CLT	25.0
HYB_e-1.1	HYB_e-1	B	CLT	25.0
HYB_e-1.2		B	CLT	25.0
HYB_e-1.3		B	CLT	37.5
HYB_e-1.4		B	CLT	37.5
HYB_e-1.5		B	CLT	37.5
HYB_s-1.1	HYB_s-1	B	no CLT	25.0
HYB_s-1.2		B	no CLT	25.0
HYB_s-1.3		B	no CLT	37.5
HYB_s-1.4		B	no CLT	37.5
HYB_s-1.5		B	no CLT	37.5

Protocol A: 1 ×5 mm+3 ×10-20-30-40-50 mm; 2 mm/s
Protocol B: 1 ×5-10 mm+3×20-40-60-80-100 mm; 2 mm/s

2.3 | Test overview

Table 2 summarizes the 20 tests that are presented in this paper. The first part of the testing campaign (on specimens with design HYB and HYB_e) was carried out on the main setup that includes the CLT panel. The last five tests, on the HYB_s specimen, were performed on the secondary setup which was made of steel and did not include the CLT panel. The labels of the tests are as follows: <name of design>-<number of sample>.<number of repetition>, so for example the label *HYB-2.3* indicates the third test on the second sample with HYB design. The preload was set initially to 25 kN per bolt, which would yield a sliding force of 20 kN, considering a 0.2 friction coefficient of aluminum. The preload value was then increased to 37.5 kN, in order to reach a sliding force of 30 kN. The preload was applied by using the torque method described in the standard EN1090-2[45] and following the specification of the bolt producer.[46]

3 | RESULTS AND DISCUSSION

Figures 9, 10, 11, 12 show the results in terms of force-displacement hysteresis loops. The overall behaviour can be assimilated to a rigid-plastic system, which would have a perfectly rectangular shape for an ideal friction connection–the loops exhibit force peaks during the initial cycles. The peaks decrease and stabilize at higher levels of displacements. This phenomenon was also observed in the previous experimental campaign due to degradation agents related to wear phenomena. Indeed the shape of the hysteresis curves tends to flatten after successive repetition on the same specimen, confirming the observed degradation. A visual inspection of the curves does not manifest meaningful differences between HYB specimens and HYB_e specimen, suggesting that the small difference in eccentricity (see Figure 4c and Table 1) does not play an essential role in the friction behaviour. Therefore, the HYB and HYB_e specimens may be considered equivalent. Interesting remarks arise by comparing the plots of the tests referred to the steel setup, shown in Figure 12, and the plots associated with the setup including the CLT panel and screw connection. In both cases, some corner chipping is present, typical of AFCs. However, the loss of energy at the change of loading direction is more prominent in the tests with the CLT panel, implying that the added deformability due to the screw connection modified the friction behaviour to a certain

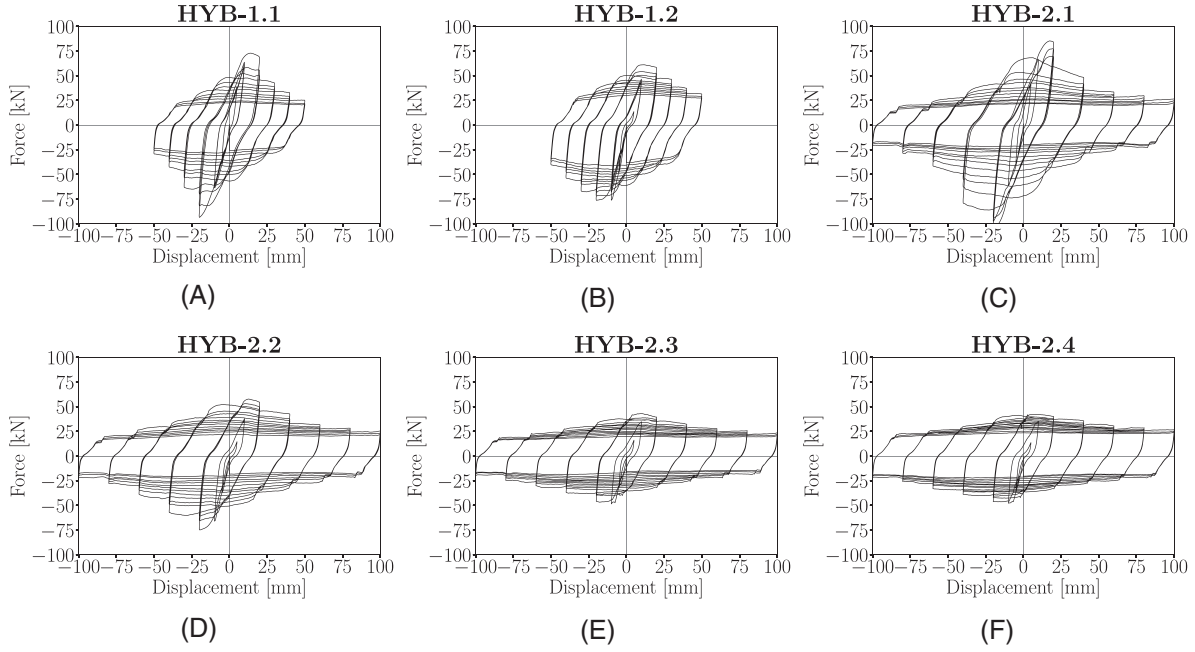

FIGURE 9 Test results of specimen HYB-1 and HYB-2, all with preload 25 kN

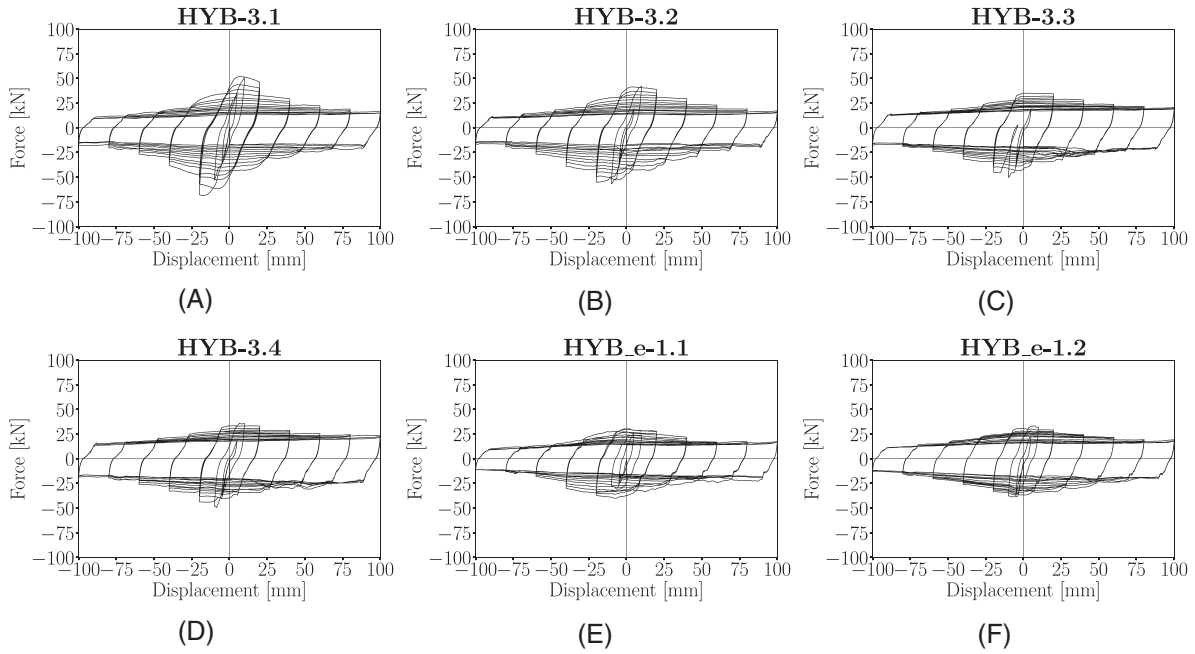

FIGURE 10 Test results of specimen HYB-3 and part of HYB_e.1, all with preload 25 kN

extent and resulted in a loss of dissipated energy. The shape is also more rectangular in the tests without CLT panels. The parts of the hysteresis curve associated with changes of load direction are almost vertical, while the tests including CLT present an S-like shape, more evident in the initial cycles, due to pinching behaviour typical of timber connections.

Table 3 presents the results as values of the slip force and friction coefficient. The authors adopted the same definition of slip force F_{slip} as,[40] which is defined as the dissipated energy E per unit of travel D:

$$E = \sum_{i=0}^{n} E_i = \sum_{i=0}^{n} \left| \frac{F_{i+1} + F_i}{2} \cdot (\delta_{i+1} - \delta_i) \right| \qquad D = \sum_{i=0}^{n} |\delta_{i+1} - \delta_i| \qquad F_{\text{slip}} = \frac{E}{D} \tag{1}$$

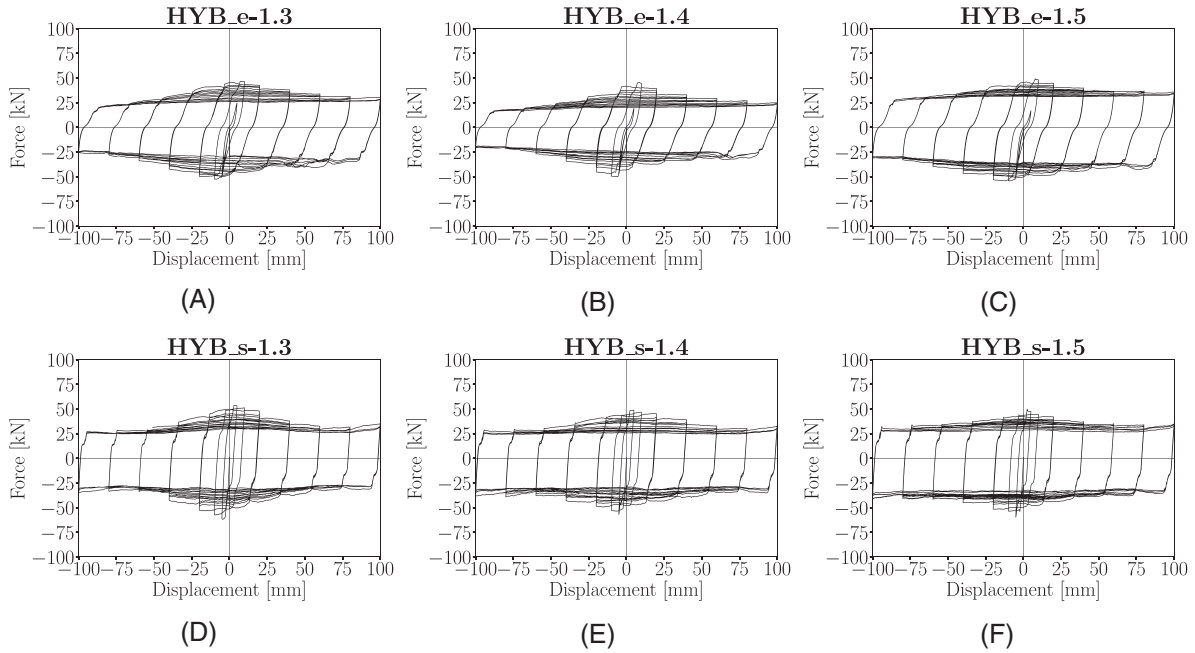

FIGURE 11 Test results for specimen HYB_e-1 HYB_s-1 with preload 37.5 V

FIGURE 12 Test results for specimen HYB_s-1 with preload 25 kN

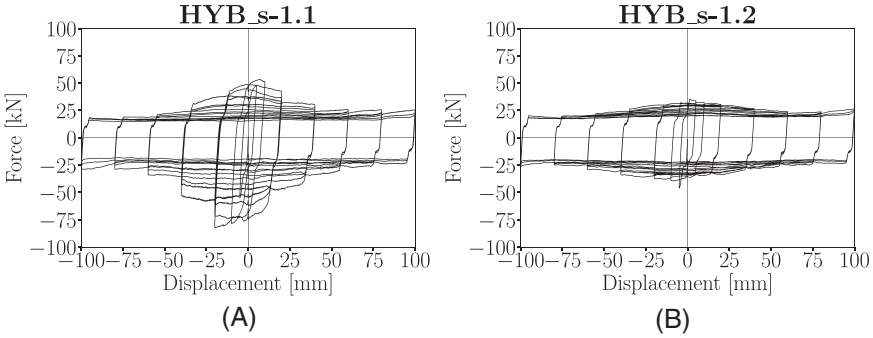

where E_i denotes the energy at the $i-$th time step, F_i and δ_i are the force and displacement at the same time step, respectively. The dissipated energy is a strictly increasing function, and is thus chosen as parameter for the evaluation of the slip force, as opposed to the force value which varies. The standard deviation and COV are calculated as follows:

$$F_{sd} = \sqrt{\frac{\sum_{i=0}^{n} |F_i - F_{\text{slip}}|^2}{n-1}} \qquad COV = \frac{F_{sd}}{F_{\text{slip}}} \tag{2}$$

This parameter synthesizes the stability of the hysteresis loops and the nature of the sliding behavior: a low value of COV corresponds to stable performance, with a loop shape more similar to the ideal rectangle. The experimental friction coefficient μ is evaluated as:

$$\mu = \frac{F_{\text{slip}}}{n_s n_b F_P} \tag{3}$$

where F_{slip} is the slip force calculated in Equation (2), $n_s = 2$ is the number of shear surfaces, $n_b = 2$ is the number of the preloaded bolts and F_P is the preload force from Table 2. It is important to note that the definition of slip force, and so the friction coefficient, is dependent on the dissipated energy and thus the displacement imposed as load protocol. Particularly in the case of shorter load protocols, considering the initial force peaks, the calculations may be inaccurate until the connection and the contact areas have stabilized, reaching the real contact area as suggested by Ref.[47] For the

TABLE 3 Results in terms of slip force, standard deviation, coefficient of variation, stability coefficient and friction coefficient

Test	F_{slip} [kN]	StDev[kN]	COV	μ
HYB-1.1	29.61	12.92	0.44	0.30
HYB-1.2	36.07	14.68	0.41	0.36
Mean				0.33
HYB-2.1	28.35	13.70	0.48	0.28
HYB-2.2	26.91	10.35	0.38	0.27
HYB-2.3	22.49	6.91	0.31	0.22
HYB-2.4	25.52	7.40	0.29	0.26
HYB-3.1	19.86	7.98	0.40	0.20
HYB-3.2	19.73	7.52	0.38	0.20
HYB-3.3	20.55	5.67	0.28	0.21
HYB-3.4	21.58	5.73	0.27	0.22
HYB_e-1.1	17.03	5.32	0.31	0.17
HYB_e-1.2	19.21	5.52	0.29	0.19
HYB_e-1.3	30.38	8.15	0.27	0.20
HYB_e-1.4	24.79	6.43	0.26	0.17
HYB_e-1.5	34.41	8.53	0.25	0.23
Mean				0.22
HYB_s-1.1	18.94	8.92	0.47	0.19
HYB_s-1.2	23.45	4.28	0.18	0.23
HYB_s-1.3	31.53	5.35	0.17	0.21
HYB_s-1.4	31.25	5.45	0.17	0.21
HYB_s-1.5	33.87	5.12	0.15	0.23
Mean				0.21

data elaboration the authors decided to use only the cycles after 20 mm, since the initial part is considered of settlement and not of real friction behavior. Furthermore, in tests including the CLT panel, the displacement adopted was purified from the effect of the timber connection by subtracting the displacement value measured by the LDT A fixed on the CLT, see Figure 7a.

The values of slip force and friction coefficient of specimen HYB-1, reported in Table 3, appear higher than all the others. These aspects confirm that the amplitude and number of the cycles strongly influence the stabilization of the friction behaviour since these tests had a shorter load protocol (see Table 2). Specimen HYB-2, HYB-3, and HYB_e all had friction coefficients in line with the expectations for aluminium shims, with an average value for the 13 tests equal to 0.22. This value is similar to the findings of the previous experimental campaign,[40] and other values in literature.[48] The tests on the specimen HYB_s, carried out on the setup without CLT panel, show similar friction coefficient values, with a 0.21 average. The friction connection behaves as predicted in both systems, suggesting that the setup, including the CLT panel, does not significantly affect the friction connection. One difference may be found in the stability of the slip force since the tests on the CLT setup generally show higher COVs than the tests on the steel set up, proving that a stiffer connection system is always preferable to obtain a stable friction behaviour. A preliminary remark regards the preloading method according to:[45] the bolts preload is applied by using a torque wrench. Therefore, the accuracy of the initial value influences the resulting slip force used to calculate the friction coefficient. The torque wrench method can be affected by a significant uncertainty due to human error. This fact can result in a preload higher than designed. A misestimation of the slip force could have occurred for specimen HYB-2, which generally has a higher friction coefficient than the other two specimens. Nevertheless, this factor is to be also expected in the building site, where many different operators could be working and installing CLT panels and friction connections. Figure 13, for tests HYB-3.1 and HYB-3.2 as an example, highlights the possible misestimation of the actual slip force, and consequently the friction coefficient, being influenced by the loading protocol and showing a decreasing trend towards their final values. In the horizontal axis, the displacement steps of the loading protocol are shown, and for each value of step, three estimates of slip force (or friction coefficient) are shown, corresponding to cycles with the same maximum displacement. A small vertical distance between the markers

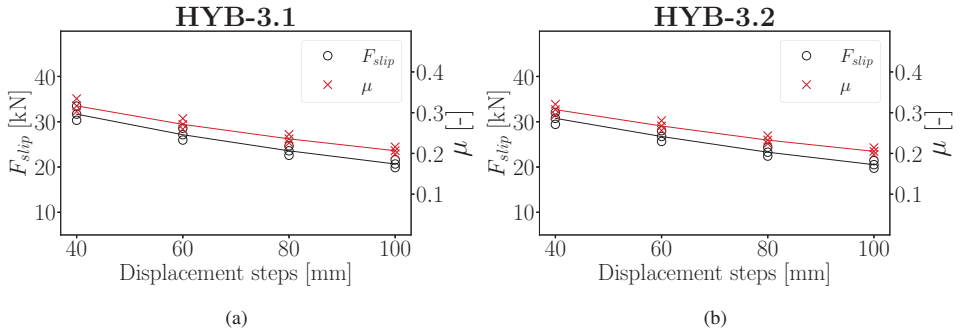

FIGURE 13 Results of specimen HYB-3, in terms of slip force and friction coefficient, (A) first and (B) second repetition

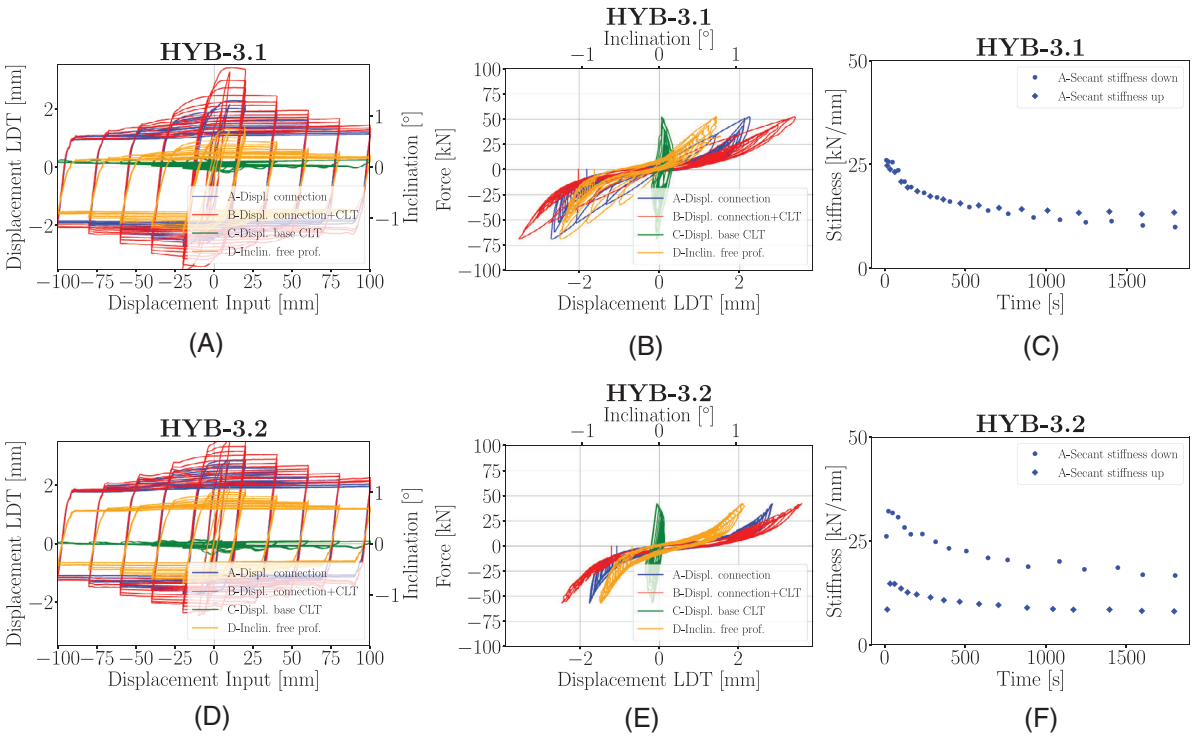

FIGURE 14 Example of results of specimen HYB-3, first and second repetition. (A) and (D) show the displacements/inclination measured by some sensors with reference to the input displacement, Figure 6 aids the reader with a labels referring to the sensors considered. (B) and (E) plot the displacements of the sensors and the measured force. (C) and (F) show an estimate of the secant stiffness of the screw connection

of the same step indicates that the slip force (or friction coefficient) was not changing between repetitions at the same displacement step. The different displacement steps show the declining trend, which tends to the final value of slip force and friction coefficient. The authors waited for each specimen to cool down before testing again. Therefore the reduction of the friction coefficient within each test depends on both the temperature rising and wear phenomena. Conversely, the initial friction coefficient, observed at each test, depends on the energy dissipated in previous tests. The variation of the friction coefficient due to temperature cannot be eliminated. However, the friction stabilization due to wear phenomena can be reduced by adequately pre-treating the shim layers before installation. Artificial wear could be generated, thus limiting the significant slip force variation.

For brevity, the data recorded by other sensors is shown for the sole HYB-3.1 and HYB.3.2 tests, see Figure 14. The plots (a) and (d) display the displacement measured by additional sensors as a function of the displacement input of the loading protocol. Sensor A is the LDT measuring the relative slip between the free profile and the CLT panel. Sensor B records the same quantity but refers to the fixed base, thus including the panel elastic deformation. Sensor C is the LDT measuring the uplift, and sensor D is the inclinometer. Figure 7 possesses the same notation. Interestingly the shape

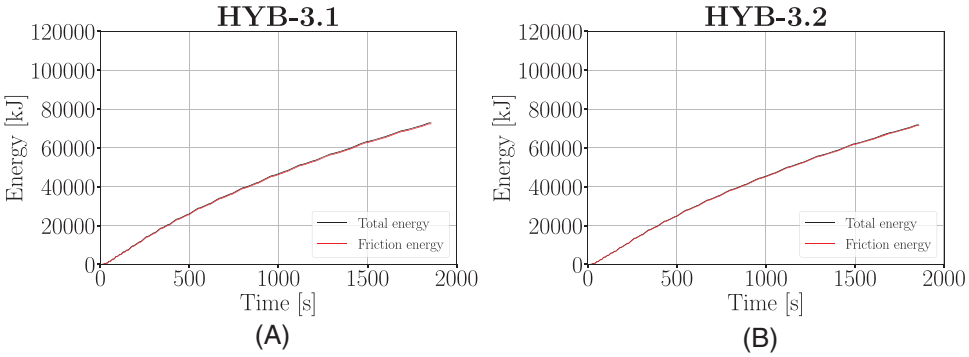

FIGURE 15 Results of specimen HYB-3, in terms of dissipated energy, (A) first and (B) second repetition

TABLE 4 Dissipated energy

Test	F_{slip} [kN]	Tot.energy [kJ]	Fric. energy [kJ]	Diff. [%]
HYB-1.1	29.61	48929.59	47763.38	2.38
HYB-1.2	36.07	56849.11	55779.93	1.88
HYB-2.1	28.35	99499.52	98067.97	1.44
HYB-2.2	26.91	94513.16	93538.26	1.03
HYB-2.3	22.49	79627.88	78952.65	0.85
HYB-2.4	25.52	89283.50	88512.00	0.86
HYB-3.1	19.86	72876.99	72361.55	0.71
HYB-3.2	19.73	71847.07	71448.99	0.55
HYB-3.3	20.55	73750.34	73356.27	0.53
HYB-3.4	21.58	76981.71	76594.24	0.50
HYB_e-1.1	17.03	62562.89	62324.80	0.38
HYB_e-1.2	19.21	69662.94	69429.91	0.33
HYB_e-1.3	30.38	107081.30	106635.93	0.42
HYB_e-1.4	24.79	88260.30	87902.15	0.41
HYB_e-1.5	34.41	119802.50	119339.37	0.39
HYB_s-1.1	18.94	91906.66		
HYB_s-1.2	23.45	86867.67		
HYB_s-1.3	31.53	116433.62		
HYB_s-1.4	31.25	115282.31		
HYB_s-1.5	33.87	124091.57		

of these curves closely follows that of the slip force, and as expected, the measure from sensor B is slightly higher than sensor A. Measures from sensor C are almost zero, confirming the adequate stiffness of the hold-down. Plots (b) and (e) use the same measurements, but with the force value on the vertical axis. In this case, the S-shape of the curves is typical of timber connections, characterized by a certain level of pinching. Plots (c) and (f) show the values of the secant stiffness of the timber connection as a function of time. The stiffness was calculated by dividing the peak force at each cycle by the corresponding measure of the LDT A. The values were plotted for each cycle, separating the downwards from the upwards direction. The graphs show that the timber connection suffers from stiffness degradation as the number of cycles increases. The value of stiffness also changes abruptly between downwards and upwards direction after the first repetition, implying an effect from the residual deformations of the first test. This asymmetric behaviour was observed for all specimens following the first repetition in all tests.

Figure 15 shows the dissipated energy for tests HYB-3.1 and HYB.3.2, while the respective estimates are reported in Table 4. The total dissipated energy, the black curve in Figure 15, was calculated using the displacement measured by the wire sensor during the tests. Parallelly, the friction energy was estimated using displacement values purged from the effect of the screw connection slip, that is, by subtracting the measure taken by sensor A. This calculation aims to isolate the

TABLE 5 Dissipated energy: comparison between the two setups

Test	F_{slip} [kN]	μ	Tot. energy [kJ]
HYB-2/3/e1.1/2	21.84	0.22	78493.76
HYB_s-1.1/2	21.20	0.21	89387.17
Diff [%]	3.08	3.97	12.19
HYB_e-1.3/4/5	29.86	0.20	105048.03
HYB_s-1.3/4/5	32.22	0.22	118602.50
Diff [%]	7.32	7.69	11.43

energy dissipation due to friction. From the plots and the values in the Table 4, it is evident that the two contributions are almost equal, with differences smaller than 3%. This fact suggests that the screw connection was stiff enough and did not reduce the energy dissipation due to friction.

This approach followed for estimating the dissipated energy due to friction, although simple, may still include other possible deformations of the CLT setup, such as elastic deformations of the CLT panel and the rotation of the screwed connection. Then, an indirect way for evaluating and separating the full effect of the CLT presence and screw connection is to compare the results between the two setups with and without the CLT. Table 5 shows the differences between the two setups in a synthetic way for the specimens with the same load protocol: the first part of the table refers to the tests with a 25 kN preload force, the second part to the tests with 37.5 kN preload force. The first line shows the mean value of the dissipated energy for the first and second repetitions of tests on the CLT setup (HYB-2.1, HYB-2.2, HYB-3.1, HYB-3.2, HYB_e-1.1, and HYB_e-1.2), while the second line lists the same quantities for the steel setup (HYB_s-1.1, HYB_s-1.2). The third line is calculated as the mean value for the third, fourth and fifth repetition of tests on the CLT setup (HYB_e-1.3, HYB_e-1.4, and HYB_e-1.5), while the fourth line is the mean for the same repetitions on the steel setup (HYB_s-1.3, HYB_s-1.4, and HYB_s-1.5). This comparison enables us to apprehend the fundamental difference between the two setups. While the differences in slip force and friction coefficient are small, minor than 4% and 8% for lower and higher preload, respectively, the difference in dissipated energy is around 12%. This result proves that the timber connection effect is a decrease in dissipated energy compared to a system where only the steel friction connection is present.

4 | HYSTERESIS MODELING

The authors modeled the experimental cyclic curves using a Duhem-class hysteresis model,[49,50] obtained from the LuGre friction model[51] by introducing a stabilization term of the Coulomb friction and eliminating the Stribeck[52] and viscosity effects which did not manifest in the experimental tests. The slip force can be expressed as:

$$f_s = k_0 z \tag{4}$$

where f_s is the slip force, k_0 is the pre-slip stiffness and z is the auxiliary inelastic displacement. The following first-order differential equation governs the evolution of the z variable:

$$\dot{z} = \dot{x}\left[1 - \left(\frac{k_0}{\mu_u h(\epsilon) F_p}\right) z \operatorname{sign}\dot{x}\right]^n \qquad h(\epsilon) \equiv \frac{\mu}{\mu_u} = 1 + \frac{\alpha}{1 + \beta\epsilon^\eta} \tag{5}$$

where x is the displacement, $\dot{x}$ the derivative of x with respect to time, F_p the preload force, μ_u the stable friction coefficient, $\alpha = \frac{(\mu_i - \mu_u)}{\mu_u} \in [0 - 1]$ expresses the relative increment of the friction coefficient at the initial stages of deformation (μ_i), β and γ define the shape of stabilization function of the friction coefficient, ϵ is the dissipated hysteretic energy. Firstly, the authors provide the motivations in choosing this particular hysteresis model, then they validate the model against the experimental data. In the last subsection, the model parameters of the chosen model are estimated from all experimental data using a genetic optimization algorithm.

4.1 | Motivation in the model selection

The dry kinetic friction, occurring in the tested specimens, can be described by the well-known Coulomb equation:

$$f_s(x, \dot{x}) = \mu F_p \text{sign}\dot{x} \tag{6}$$

where μ is the friction coefficient. However, the basic Coulomb model suffers from two severe limitations. It does not model the pre-slip stiffness and it cannot reproduce the corner chipping effect, often significant in friction connections. The pre-slip stiffness derives from the intrinsic deformability of the connection and the shim layers, which deform before the slip triggering. The chipping effect, consisting in the corner smoothing of the hysteresis curve in the un-loading phase also depends on both the shim material and the connection. They exhibit a force delay in the unloading phases, at the first stages of the reversing of the load protocol.

The Coulomb friction model may therefore not be accurate, and the classical Bouc-Wen model could be a valid alternative.[53,54] Besides, the most used hysteresis model in structural dynamics is the Bouc-Wen, which can reproduce multiple hysteresis phenomena.[55] For a structural element described by a Bouc–Wen class model, the force is written as

$$f_s(x, \dot{x}, z) = \alpha k_0 x + (1 - \alpha) k_0 z \tag{7}$$

where α the post-to-preyield stiffness ratio, and k_0 the initial stiffness. In friction connections α is generally very low, since there are no hardening phenomena. The evolution of z is determined by an auxiliary ordinary differential equation

$$\dot{z} = \dot{x}[A - |z|^n \psi(x, \dot{x}, z)] \tag{8}$$

where $\dot{z}$ is the derivative of z with respect to time, A a parameter that controls the scale of the hysteresis loops, n controls the sharpness of the hysteresis loops, and $\psi(x, \dot{x})$ a nonlinear function determining other shape features of the hysteresis loop. However, the ψ functions of the original Bouc–Wen model, and the subsequent model developments, like the ones proposed Wang and Wen,[56] Song,[57] Aloisio,[58] are not especially suited for friction connections since they do not possess an explicit dependence on the friction coefficient and the pre-loading force.

Therefore, the Dahl friction model,[59] equivalent to the Bouc-Wen model for $n = 1$, is the usual choice in friction modelling. The first-order differential equation governing the evolution of the inelastic displacement in the Dahl friction model is

$$\dot{z} = \dot{x}[1 - z\ \text{sign}\dot{x}]^n \tag{9}$$

However, also this model, generally used in friction modelling, does not possess an explicit dependence on the slip force, which must be calibrated by varying the n parameter.

The most general friction model is the LuGre one,[51] which originate from the Dahl model and captures the Stribeck ("stick-slip") effect.[60,61] This model explicits both the Coulomb sliding friction force, and the Stribeck sticking friction force. The following set of equations governs the LuGre model:

$$\dot{z} = \dot{x}\left[1 - z\,\frac{\text{sign}\dot{x}}{g(\dot{x})}\right]^n \qquad k_0 g(\dot{x}) = F_c + (F_s - F_c)\mathrm{e}^{(-\dot{x}/v_s)} \qquad f_s = k_0 z + c_1 \dot{z} + c_2 \dot{x} \tag{10}$$

where c_1 is friction rate effect, c_2 is viscous rate effect, F_c is the Coulomb sliding friction force, F_s is the Stribeck sticking friction force, v_s the Stribeck velocity.

However, the current experimental tests did not evidence the Stribeck phenomenon and manifested a reduction of the friction coefficient as the number of cycles increased. Therefore, the authors adopted the LuGre model with the following upgrades and simplifications: the Coulomb sliding friction force is set equal to the Stribeck sticking friction force, since there are no stick-slip phenomena, and the rate coefficients c_1 and c_2 are set equal to zero, since the tests are quasi-static and the viscous phenomena are negligible.

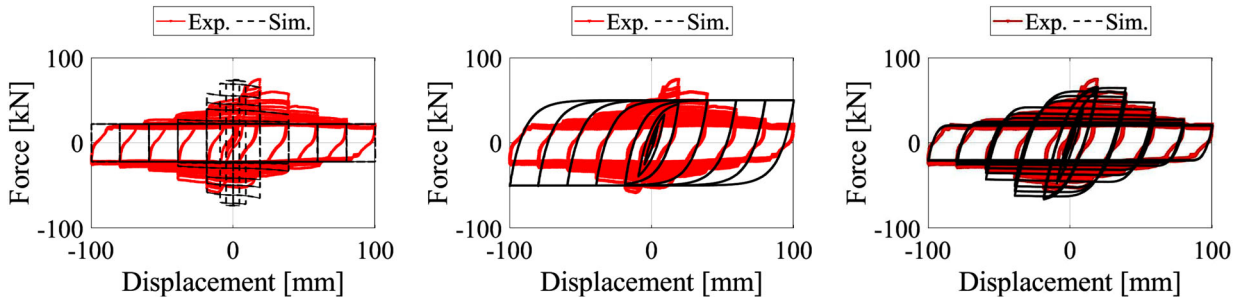

FIGURE 16 Comparison between three hysteresis model in fitting the experimental data of the HYB-2.1 test. The first is the Coulomb model with degradation proposed by Ref.,[40] the second is the classical Bouc-Wen model, the third is the one implemented in this research shown in Equation 5

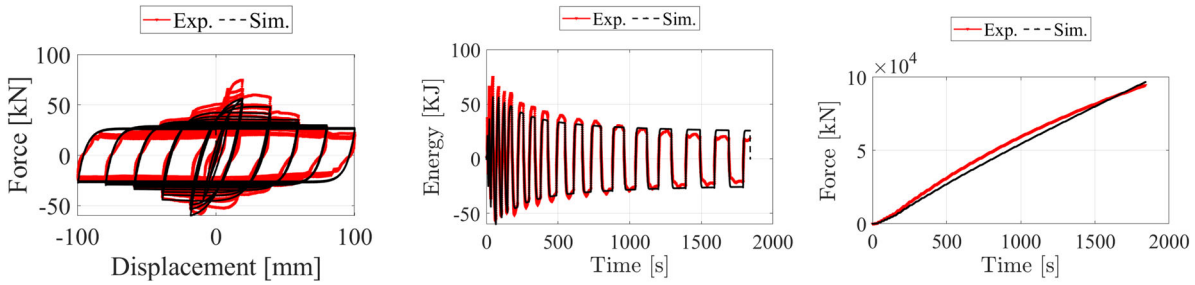

FIGURE 17 Comparison between the experimental and simulated data in terms of force-displacement, force-time and energy-time functions for the HYB-2.1 test

The evolution of the friction coefficient is achieved by adopting a stabilization function, dependent on the dissipated hysteretic energy. Initially the authors adopted an exponential function, as they did in Ref.[40] However, the exponential function hardly follows the evolution of the friction coefficient observed in the experimental tests. Accordingly, following the well-known formulation by Ref.[62] of the degradation function, the authors observed that the stabilization function closely follows a hyperbolic evolution. Figure 16 shows the comparison between experimental data and all three possible modeling approaches presented above. In conclusion, a modification of the LuGre friction model, shown in Equation 5, rather than the Bouc-Wen model, is adopted for three main reasons. (i) The LuGre model is is among the most general models in trybology and possesses an explicit dependence on the mechanical parameters (the pre-load force and the friction coefficients, e.g.,). (ii) On the contrary, the classical Bouc-Wen model, despite capable of mirroring a wide range of hysteretic phenomena, is characterized by multiple variable with no direct physical meaning. (iii) Additionally, the parameters of the Bouc-Wen model are redundant, since multiple combination of them can shape the same hysteresis curve.[63]

4.2 | Model validation and parameter estimation

Figure 17 plots the comparison between the experimental and simulated hysteresis curves using Equation 5 in terms of force-displacement, force-time and energy-time functions. The superposition is very accurate, despite the limits and reduced number of parameters. However, the model has two primary weaknesses: the hysteresis model cannot mirror (i) possible asymmetries in the hysteresis curve and (ii) the peculiar S-like shape during the first stages of loading due to the pinching between the screws and the CLT specimen. However, these two phenomena are not very influential to the structural performance of the AFC. Besides, the asymmetries in the loop should be absent in an actual case application. Though, in the current setup, the CLT specimens are restrained by a hold-down, causing asymmetries in the response. However, despite these two limits, the chosen model accurately seizes the stabilization of the slip force, and the estimated dissipated energy almost overlaps with the experimental curve.

The authors repeated the fitting to all test data and estimated the parameters using a genetic optimization algorithm. Specifically, the experimental force-displacement data are used to calibrate the hysteresis model parameters. The cal-

TABLE 6 Optimum parameters of the hysteresis model in Equation 5 for each data set

Label	k_0 [kN/mm]	μ	n	α	β	η
HYB-1.1	5.95	0.25	0.89	4.63	2.19E-07	0.9745
HYB-1.2	5.86	0.30	0.97	2.64	1.86E-07	0.9364
HYB-2.1	5.11	0.22	0.89	4.99	1.17E-07	0.9738
HYB-2.2	5.25	0.26	0.96	4.85	9.57E-08	0.9692
HYB-2.3	4.57	0.22	0.98	3.47	2.57E-07	0.8998
HYB-2.4	4.06	0.29	0.94	1.99	9.57E-08	0.9306
HYB-3.1	5.51	0.22	0.82	4.30	1.66E-07	0.9602
HYB-3.2	5.29	0.23	0.97	4.97	2.32E-07	0.9692
HYB-3.3	5.29	0.28	0.88	1.68	1.03E-07	0.9664
HYB-3.4	4.53	0.28	0.81	1.89	5.25E-07	0.8742
Mean	5.14	0.26	0.91	3.54	2.00E-07	0.95
Variance	0.36	1.13E-03	3.76E-03	1.89	1.67E-14	1.21E-03
HYB_e-1.1	5.64	0.22	1.00	2.47	9.23E-08	1.0000
HYB_e-1.2	5.54	0.24	0.99	2.18	1.16E-07	0.9624
HYB_e-1.3	5.44	0.20	0.84	2.22	2.28E-07	0.8601
HYB_e-1.4	5.26	0.24	0.72	1.53	2.97E-07	0.9039
HYB_e-1.5	5.89	0.22	0.65	1.80	4.50E-07	0.7828
Mean	5.55	0.23	0.84	2.04	2.37E-07	0.90
Variance	0.06	1.99E-04	0.02	0.14	2.12E-14	0.01
HYB_s-1.1	14.50	0.20	0.91	4.79	9.49E-08	0.9226
HYB_s-1.2	14.00	0.22	1.00	1.34	8.76E-07	0.7640
HYB_s-1.3	15.29	0.21	0.97	1.27	5.63E-08	0.8946
HYB_s-1.4	15.49	0.23	0.76	1.70	3.32E-08	0.9604
HYB_s-1.5	19.42	0.15	0.98	3.11	2.94E-07	0.7909
Mean	15.74	0.20	0.92	2.44	2.71E-07	0.87
Variance	4.59	1.04E-03	0.01	2.28	1.25E-13	0.01

ibration was performed by using the function GA (Genetic Algorithm) of the global optimization toolbox of software MATLAB.[64,65] The genetic algorithm performs iteration of parameters with the goal of minimizing the following objective function:

$$\text{obj}(\mathbf{p}) = \frac{\sum_{i=1}^{N} |[F_{ei} - F_{si}(\mathbf{p})]\Delta x_i|}{\sum_{i=1}^{N} |F_{ei}\Delta x_i|} \tag{11}$$

where N is the number of data points, $\mathbf{p}$ is the parameter vector containing the hysteresis model parameters, F_{ei} and Δx_i are the experimental data in terms of force and displacement increment respectively and $F_{si}(\mathbf{p})$ is the restoring force of the system simulated with the hysteresis model. Note that the objective function is defined as normalized integral of the difference between experimental force and simulated force. This gives a measure of discrepancy between experimental data and model simulation. The optimization was carried out by defining appropriate lower and upper bounds for the model parameters, based on the physical interpretation of each of them, see Table 6. The parameters and their ranges of variations are: k_0, μ_u, n, α, β, and η.

The comparison between the experimental and simulated hysteresis curves in terms of force-displacement, force-time and energy-time functions are shown in the supplementary material. The plots confirm the satisfactory matching between experimental and simulated data anticipated in Figure 17. Table 6 is organized in three sections, referring to the three tested specimens. The parameters optimization reveals that the screwed connection significantly reduces the pre-slip stiffness from approximately 15 kN/mm to almost 5 kN/mm. The effect of a lower eccentricity in the HYB_e typology possibly results in a minor increment of the pre-slip stiffness.

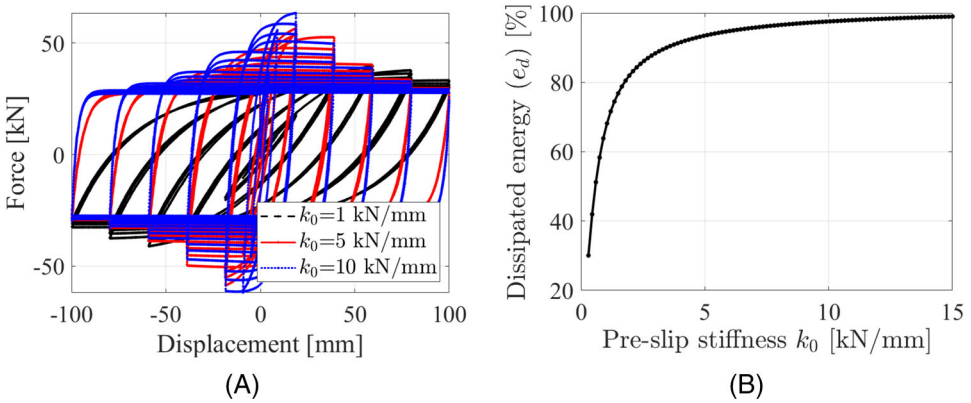

FIGURE 18 (A) Superposition of hysteresis cycles for different pre-slip stiffess values, (B) estimate of the percentage dissipated energy, $e_d = \frac{E_d}{E_{d,\infty}}$, where $E_{d,\infty}$ is the dissipated energy corresponding to $k_0 \to \infty$

The stable friction coefficient, that is, the friction coefficient corresponding to the stable cycles, is quite variable, especially after repetitions of the loading protocols. However, it is on average 0.26 for the HYB specimen and 0.23 for HYB_e. It confirms that a lower eccentricity reduces the slip force due to the lacking of parasite bending effects. The average friction coefficient reduces to 0.20 if there is no screwed connection. It may depend on possible lower eccentricity effects, which determine higher slip loads associated with uneven stress distribution. This is coherent with the findings from the experimental tests, even if these values are generally slightly higher due to the fact the LuGre model is fitted to the complete test, without excluding the initial cycles and LDT A measure as was done in the experimental part. The n exponent is not very sensitive to the test data since the shape of the hysteresis loop is comparable between tests. The α, and β and η parameters are not highly variable between test data and depend on the friction coefficient evolution as the dissipated energy grows. Therefore, for engineering purposes, the practitioner can use the mean values of the obtained parameters to represent the response of each AFC typology reliably.

5 | ESTIMATE OF THE PRE-SLIP STIFFNESS EFFECT

As discussed in Ref.,[40] the e-CLT system experiences two phases: the stick and the slip phases. During the stick phase, the AFC does not activate, and the total resisting force at the i-th story (f_t) is the summation of the resisting forces of the CLT panel (f_{clt}) and the RC frame (f_{rc}). If the reaction of the CLT panel exceeds the slip force (f_s), the AFC activates, and the total resisting force is the summation of the resisting force of the RC frame and the slip force of the AFC. The e-CLT unit behaves like a parallel system, whose governing equations are:

$$f_t = f_{\text{rc}} + f_{\text{clt}} \quad \text{if} \quad |f_{\text{clt}}| \leq |f_s| \tag{12}$$

$$f_t = f_{\text{rc}} + f_s \quad \text{if} \quad |f_{\text{clt}}| > |f_s| \tag{13}$$

The conditional statement on the exceeding of the slip force drives the transition between the two stick and slip phases of the response. Given the lateral pre-slip stiffness of the whole system comprising CLT panel-screw connection-steel plates (k_0), the conditional statement can be written in term of the displacement associated with the AFC activation:

$$d_{\text{act}} = \frac{|f_s|}{|k_0|} \tag{14}$$

Ideally, the AFC should be undeformable and, if the resisting force attains the slip force, the AFC activates. However, the AFC possesses a pre-slip stiffness (k_0), due to the deformability of the steel profiles and the screw connection. Therefore, the AFC deformation is needed to attain the required slip force level.

Figure 18a shows the superposition between three simulated hysteresis curves obtained by varying the pre-slip stiffness. Figure 18b displays the evolution of the percentage dissipated energy, $e_d = \frac{E_d}{E_{d,\infty}}$, where E_d is the dissipated energy and $E_{d,\infty}$ is the dissipated energy corresponding to $k_0 \to \infty$.

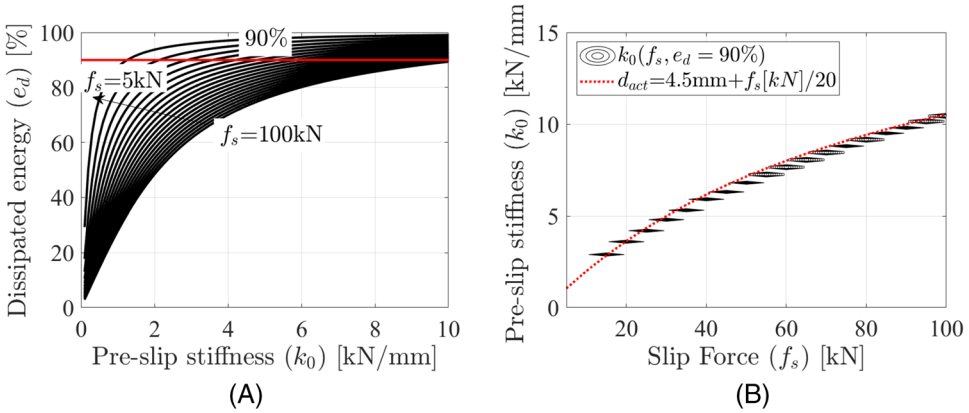

FIGURE 19 (A) Estimate of the percentage dissipated energy for different slip force values, (B) pre-slip stiffness versus slip force for 90% of dissipated energy

The increment of the total dissipated energy is not linear, and tends to an horizontal asymptote. The curve shows a clear bend for a pre-slip stiffness approximately equal to 5 kN/mm, when $e_d = 90\%$. The percentage difference between the dissipated energy with and without CLT panel is approximately 12%, as shown in Table 5 in the previous section. Therefore, Figure 18 is coherent with the experimental findings since it proves that with the considered CLT specimens, the 90% of the dissipation potential is exploited. Consequently, an approximate 10% difference between the cases with and without the CLT specimens is expected. A pre-slip stiffness lower than 5 kN/mm leads to a dramatic reduction of the dissipation potential. A pre-slip stiffness higher than 5 kN/mm does not cause a meaningful increment of the dissipated energy. Therefore, for a slip force equal to approximately 20 kN, the lateral stiffness of the slip connection should not be lower than 5 kN/mm.

More generally, in terms of displacement, the activation displacement of the tested AFC (d_{act}) should be:

$$d_{\text{act}} < \frac{f_s}{k_0} \approx \frac{20}{5} = 4\text{mm} \;\text{ if } f_s = 20\text{kN} \tag{15}$$

This optimal threshold is valid for an AFC with an approximate 20 kN slip force.

The authors simulated the cyclic response of different AFCs by varying both the slip force and the pre-slip stiffness to possibly derive a general design rule for the prediction of the minimum activation displacement corresponding to a correct design. Figure 19a shows the dissipated energy in percentage e_d, as the ratio between the dissipated energy E_d and the maximum dissipated energy ($E_{d,\infty}$) associated to a pre-load stiffness $k_0 \to \infty$. The chosen normalization of E_d allows the simultaneous plotting of curves related to different slip forces. The authors will assume that the optimal AFC performance is associated with a dissipation potential (e_d) equal to 90%. Interestingly, the values of the pre-slip stiffness, corresponding to the intersection between the e_d-k_0 curves and the horizontal threshold at 90%, plotted against the slip forces do not follow a straight line, see Figure 19b. Therefore, the estimate of the activation displacement equal to 4 mm, valid for $f_s = 20kN$, would lead to an overestimation of the pre-slip stiffness. The authors fitted the values of $e_d \approx 90\%$ using a nonlinear least-squares optimization and obtained the following expression for the activation displacement, plotted in Figure 19b:

$$d_{\text{act}} = \frac{f_s}{k_0} \approx 4.5\text{mm} + \frac{f_s[\text{kN}]}{20} \tag{16}$$

The activation displacement should rise linearly to the slip force, as the slip force grows. This phenomenon is related to peculiar shape of the hysteresis loop. The maximization of the area inside the loop entails the contemporary increment of the activation displacement as the slip force grows.

In conclusion, the correct design of the AFC requires the estimation of the slip force and the pre-slip stiffness. The slip force derives from the structural design, while the pre-slip stiffness can be determined from Equation 16, which provides the activation displacement as a function of the slip-force.

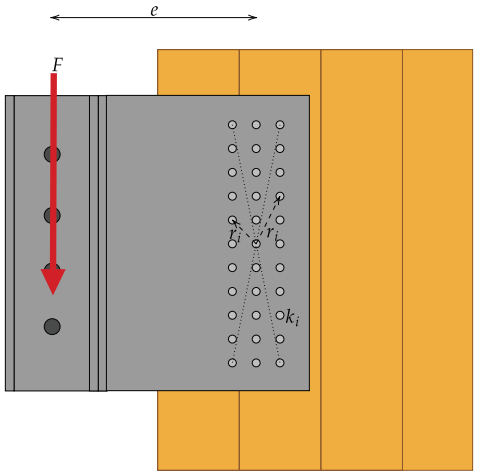

FIGURE 20 Scheme for the evaluation of the stiffness

5.1 | Lateral stiffness of the screw connection

Theoretically, the design pre-slip stiffness can be obtained by using an adequate number and arrangement of screws. However, the pre-slip stiffness is also strongly affected by the intrinsic deformability of the AFC layout rather than only by the screw connection. In this subsection, the contribution of pre-slip stiffness due to the screws has been isolated. The experimental lateral stiffness of the screw connection is compared to the estimates according to the Eurocode 5 and a recent formulation by Ref.[66] According to the current Eurocode[67] the slip modulus (K_{ser}) per shear plane per fastener under service load for joints made with dowel-type fasteners is related to the mean density ρ_m and the diameter d by the first formula of Equation 17. The current formulation lacks parameters such as the length of penetration of the screw into the timber members. An alternative approach to the problem was proposed by Ref.,[68] in this case the formulation for the slip modulus was derived from an analytical model that considers the screw as a rigid body on elastic springs. Simplified but more accurate formulas to predict the sliding modulus starting from the geometric characteristics and timber member densities of the connection has been derived by Ref.[66] This approach, seen in the second formula of Equation 17, are based on an analytical model of beam on elastic foundation taking into account the timber anisotropy and the axial and bending stiffness of the screws:

$$k_{i,EC5} = 2\rho_m^{1.5} d_{ef}/23 \qquad k_{i,DS} = 0.44\rho_m^{1.02} l_p^{0.075} d_{ex}^{1.24} \tag{17}$$

where ρ_m is the mean timber density in kg/m^3, d_{ex} is the outer thread diameter, l_p is the length of penetration of the screw into the CLT panel and $d_{ef} = 1.1 d_{in}$ where d_{in} is the screw thread root diameter. The total stiffness of the connection was calculated as an equivalent spring that takes into account the rotational effect of the eccentricity as follows (see also Figure 20):

$$K_e = \frac{1}{\frac{1}{K_v} + \frac{e^2}{K_r}} \qquad K_v = \sum_{i=1}^{n_s} k_i \qquad K_r = \sum_{i=1}^{n_s} k_i r_i^2 \tag{18}$$

where K_e is the stiffness of the connection evaluated in a point of eccentricity e with respect to the center of rotation of the connection (center of the screws), k_i is the slip modulus of the i^{th} screw, K_v is the equivalent translational slip modulus of all screws, n_s is the number of screws, K_r is the equivalent rotational slip modulus of all screws and r_i is the distance of the i^{th} screw to the center of rotation.

The experimental estimates in Table 7 are calculated as secant values for the first repetition on each specimen, calculated as the average value of the first cycles up to 20 mm. Table 8 shows a comparison between the experimental secant stiffness and the two analytical formulations. The comparison proves that the formulation from Ref.[66] is closer to the experimental one.

However, the experimental estimates and the predicted values significantly exceed the pre-slip stiffness of the considered AFC connections. Therefore, the design value of the pre-slip stiffness cannot be obtained directly by varying the

TABLE 7 Experimental secant stiffness

Test	K^e [kN/mm]
HYB-1.1	31.50
HYB-2.1	32.34
HYB-3.1	24.67
HYB_e-1.1	22.84
Mean	27.84
St.Dev	4.14

TABLE 8 Stiffness values comparison, values in [kN/mm]

Experimental	De Santis[66]	EC5
27.84	31.74	38.29

number and arrangement of the screws. The geometry of the AFC and its layout significantly affects the overall deformability, since the sole stiffness of the screws is five times higher than the pre-slip stiffness of the whole system. Accordingly, the pre-slip stiffness should be estimated from a detailed FE model of the connection or experimental test of the complete system configuration, rather than an analytical estimate of the stiffness of the screwed connection from technical standards or well-acknowledged formulations.

6 | CONCLUSIONS

This paper presents the experimental results of cyclic tests on a particular class of AFC attached to CLT panels. Following the experimental campaign by Boggian et al.,[40] this paper investigates the effect of the screw connection, connecting the AFC to the CLT panel, on the friction performance of the AFC. The main effect of the screw connection is the reduction of the pre-slip stiffness of the AFC. The experimental tests also confirmed the findings by multiple researchers on this topic. The friction coefficient of the AFC tends to stabilize after multiple cycles, possibly due to wear phenomena between the aluminum shims and the steel plates, to an average value of 0.22. Future research will aim at improving the friction coefficient stability by reducing the consequences of wear phenomena by proper pre-treatment of the shim layers surfaces. The effect of the pre-slip stiffness on the AFC performance has been estimated by developing a novel analytical hysteresis model for AFC, obtained from a modification of the Lu-Gre model. The friction coefficient evolution is obtained by adopting a hyperbolic energy-dependent term. The model leads to a satisfactory agreement between experimental and simulated data. Furthermore, the model has been calibrated using a genetic optimization algorithm implemented in Matlab. The proposed model is then used to estimate the effect of the pre-slip stiffness on the AFC performance. The analysis shows that in the considered setup, the AFC with the CLT panel leads to a 90% exploitation of the maximum dissipation potential of the AFC, in full agreement with the experimental results. The maximum dissipated energy corresponds to a pre-slip stiffness tending to infinity. The role of the pre-slip stiffness is crucial to reach optimal energy dissipation. Therefore, the designer must select the pre-slip stiffness and the slip force to maximize the dissipation potential. In the considered specimen, the pre-slip stiffness should not be lower than 5 kN/mm to achieve a 90% of the dissipation potential. The pre-slip stiffness strongly depends on the friction system geometry rather than solely on the number and arrangement of screws. The experimental and analytical estimates of the lateral stiffness of the screwed connection significantly exceed the pre-slip stiffness. Therefore, the number and arrangement of screws are not the sole design parameter for increasing the design pre-slip stiffness. The designer must develop a detailed model of the complete AFC system to provide a reliable estimate of the pre-slip stiffness.

ACKNOWLEDGEMENTS

The authors would like to thank Scott Brenna, Frode Røsstad, Matteo Manghi, Roar Økseter and Øyvind Hansen for their precious contribution during the testing activity. This paper was carried out in the framework of the "Energy and seismic affordable renovation solutions" (e-SAFE) project, which has received funding from the European Union's Horizon 2020 research and innovation programme under grant agreement No.893135. Neither the Executive Agency for Small and

Medium-sized Enterprises (EASME) nor the European Commission is in any way responsible for any use that may be made of the information it contains.

DATA AVAILABILITY STATEMENT

The data that support the findings of this study are available from the corresponding author upon reasonable request.

ORCID

Francesco Boggian https://orcid.org/0000-0002-1039-386X
Angelo Aloisio https://orcid.org/0000-0002-6190-0139
Roberto Tomasi https://orcid.org/0000-0001-8002-8481

REFERENCES

1. White DW, Duk Kim Y. Unified flexural resistance equations for stability design of steel I-section members: moment gradient tests. *J Struct Eng*. 2008;134(9):1471-1486.
2. Priya DS, Cinitha A, Umesha P, Iyer NR. A critical review on enhancing the seismic response of buildings with energy dissipation methods. *J Struct Eng*. 2015;42(3):78-88.
3. Spencer Jr B, Nagarajaiah S. State of the art of structural control. *J Struct Eng*. 2003;129(7):845-856.
4. Habibi A, Chan RW, Albermani F. Energy-based design method for seismic retrofitting with passive energy dissipation systems. *Eng Struct*. 2013;46:77-86.
5. Saaed TE, Nikolakopoulos G, Jonasson JE, Hedlund H. A state-of-the-art review of structural control systems. *J Vib Control*. 2015;21(5):919-937.
6. Jaisee S, Yue F, Ooi YH. A state-of-the-art review on passive friction dampers and their applications. *Eng Struct*. 2021;235:112022.
7. Cardone D, Dolce M, Ponzo FC, Coelho E Experimental behaviour of R/C frames retrofitted with dissipating and re-centring braces. *J Earthquake Eng*. 2004;8(03):361–396.
8. Chen WF, Lui EM. *Handbook of Structural Engineering*. CRC press; 2005.
9. Pall AS, Marsh C. Response of friction damped braced frames. *J Struct Div*. 1982;108(6):1313-1323.
10. Pesaresi L, Stender M, Ruffini V, Schwingshackl C. DIC measurement of the kinematics of a friction damper for turbine applications. In: Springer 2017:93-101.
11. Csaba G. Modelling of a microslip friction damper subjected to translation and rotation. *Proceedings of the ASME Turbo Expo*. 1999; 4:https://doi.org/10.1115/99-GT-149
12. Pall AS, Marsh C. FRICTION-DAMPED CONCRETE SHEARWALLS. *J Am Concrete Ins*. 1981;78(3):187–193.
13. Pall AS. Friction devices for aseismic design of buildings. In: 1983:475-484.
14. Pasquin C, Leboeuf N, Pall T Friction dampers for seismic rehabilitation of Eaton Building, Montreal. Proceedings, Annual Conference - Canadian Society for Civil Engineering, 2002, 2002; pp. 1771–1780.
15. Chandra R, Masand M, Nandi S, Tripathi C, Pall R, Pall A. Friction-dampers for seismic control of La Gardenia towers south city, Gurgaon, India. In: 2000.
16. Pall A, Vezina S, Proulx P, Pall R. Friction-dampers for seismic control of Canadian space agency headquarters. *Earthq Spectra*. 1993;9(3):547-557.
17. Wu B, Li H, Lin L, Shan M. Seismic retrofit of a city hall in Northeast China with frictional energy dissipators. *J Build Struct*. 1998;19(5):28-36.
18. Wu B, Zhang J, Williams M, Ou J. Hysteretic behavior of improved Pall-typed frictional dampers. *Eng Struct*. 2005;27(8):1258-1267.
19. Filiatrault A, Cherry S. Performance evaluation of friction damped braced steel frames under simulated earthquake loads. *Earthq Spectra*. 1987;3(1):57-78.
20. Fitzgerald T, Anagnos T, Goodson M, Zsutty T. Slotted bolted connections in aseismic design for concentrically braced connections. *Earthq Spectra*. 1989;5(2):383-391.
21. Latour M, Rizzano G, Santiago A, Silva dLS. Experimental response of a low-yielding, self-centering, rocking column base joint with friction dampers. *Soil Dyn Earthq Eng*. 2019;116:580-592.
22. Loo WY, Quenneville P, Chouw N. A new type of symmetric slip-friction connector. *J Constr Steel Res*. 2014;94:11-22.
23. Khoo HH, Clifton C, MacRae G, Zhou H, Ramhormozian S. Proposed design models for the asymmetric friction connection. *Earthq Eng Struct Dyn*. 2015;44(8):1309-1324.
24. Khoo HH, Clifton C, Butterworth J, MacRae G, Ferguson G. Influence of steel shim hardness on the Sliding Hinge Joint performance. *J Constr Steel Res*. 2012;72:119-129.
25. Kim HJ, Christopoulos C. Friction damped posttensioned self-centering steel moment-resisting frames. *J Struct Eng*. 2008;134(11):1768-1779.
26. Rad AA, MacRae GA, Hazaveh NK, Ma Q. Shake table testing of a low damage steel building with Asymmetric Friction Connections (AFC). *J Constr Steel Res*. 2019;155:129-143.
27. Khoo HH, Clifton C, Butterworth J, MacRae G. Experimental study of full-scale self-centering sliding hinge joint connections with friction ring springs. *J Earthq Eng*. 2013;17(7):972-997.
28. Chanchi Golondrino JC, MacRae GA, Chase JG, Rodgers GW, Clifton GC. Seismic behaviour of symmetric friction connections for steel buildings. *Eng Struct*. 2020;224:111200. https://doi.org/10.1016/j.engstruct.2020.111200

29. Loo WY, Quenneville P, Chouw N. A numerical study of the seismic behaviour of timber shear walls with slip-friction connectors. *Eng Struct*. 2012;34:233-243. https://doi.org/10.1016/j.engstruct.2011.09.016
30. Loo W, Quenneville P, Chouw N. A new type of symmetric slip-friction connector. *J Constr Steel Res*. 2014;94:11-22. https://doi.org/10.1016/j.jcsr.2013.11.005
31. Loo WY, Kun C, Quenneville P, Chouw N. Experimental testing of a rocking timber shear wall with slip-friction connectors. *Earthq Eng Struct Dyn*. 2014;43(11):1621-1639. https://doi.org/10.1002/eqe.2413
32. Loo WY, Quenneville P, Chouw N. Rocking timber structure with slip-friction connectors conceptualized as a plastically deformable hinge within a multistory shear wall. *J Struct Eng*. 2016;142(4):E4015010. https://doi.org/10.1061/(ASCE)ST.1943-541X.0001387
33. Fitzgerald D, Sinha A, Miller TH, Nairn JA. Axial slip-friction connections for cross-laminated timber. *Eng Struct*. 2021;228:111478. https://doi.org/10.1016/j.engstruct.2020.111478
34. Fitzgerald D, Miller TH, Sinha A, Nairn JA Cross-laminated timber rocking walls with slip-friction connections. *Eng Struct*. 2020;220:110973.
35. Björnfot A, Boggian F, Nygård A, Tomasi R. Strengthening Of traditional buildings with slim panels of Cross-Laminated Timber (CLT). In: International Conference on Structural Health Assessment of Timber Structures; 2017.
36. Sustersic I, Dujic B. Seismic strengthening of existing URM and RC structures using Xlam timber panels. In: International conference on Earthquake Engineering; 2013.
37. Stazi F, Serpilli M, Maracchini G, Pavone A. An experimental and numerical study on CLT panels used as infill shear walls for RC buildings retrofit. *Constr Build Mater*. 2019;211:605-616. https://doi.org/10.1016/j.conbuildmat.2019.03.196
38. Tardo C, Boggian F, Hatletveit M, Marino E, Margani G, Tomasi R. Mechanical characterization of energy dissipation devices in retrofit solution of reinforced concrete frames coupled with solid wood panels. In: Proceedings of the 12th International Conference on Structural Analysis of Historical Constructions; 2020.
39. Margani G, Evola G, Tardo C, Marino EM. Energy, seismic, and architectural renovation of RC framed buildings with prefabricated timber panels. *Sustainability*. 2020;12(12):4845. https://doi.org/10.3390/su12124845
40. Boggian F, Tardo C, Aloisio A, Marino EM, Tomasi R Experimental cyclic response of a novel friction connection for seismic retrofitting of RC buildings with CLT panels. *J Struct Eng*. 2022;148(5):04022040.
41. Tardo C. *Seismic and Energy Renovation of RC Framed Buildings with Cross-Laminated Timber Panels Equipped with Innovative Friction Dampers*. PhD thesis. University of Catania, Italy; 2021.
42. EN14399-4. High-strength structural bolting assemblies for preloading - Part 4: System HV - Hexagon bolt and nut assemblies. 2015.
43. Rothoblaas. SCREWS AND CONNECTORS FOR WOOD-CARPENTRY, STRUCTURES AND OUTDOOR. Accessed: January 12, 2022. https://www.rothoblaas.it/cataloghi/27-viti-e-connettori-per-legno?action=download&lang=en
44. EN15129. Anti-seismic devices. 2018.
45. EN1090-2. Execution of steel structures and aluminium structures - Part 2: Technical requirements for steel structures. 2018.
46. SBE-Varvit. STRUCTURAL BOLTING ASSEMBLIES EN 14399 PRELOADED ASSEMBLIES. Accessed: January 12, 2022. https://secure.varvit.com/pdf/EN14399.pdf
47. Bowden FP, Bowden FP, Tabor D. *The Friction and Lubrication of Solids*. Vol. 1. Oxford University Press; 2001.
48. Golondrino JC, MacRae G, Clifton C Behaviour of asymmetrical friction connections using different shim materials. In Proceedings of the New Zealand society for earthquake engineering conference. 2012.
49. Duhem P. Die dauernden Aenderungen und die Thermodynamik. I. *Z Phys Chem*. 1897;22(1):545-589.
50. Hassani V, Tjahjowidodo T, Do TN. A survey on hysteresis modeling, identification and control. *Mech Syst Sig Process*. 2014;49(1-2):209-233.
51. De Wit CC, Olsson H, Astrom KJ, Lischinsky P. A new model for control of systems with friction. *IEEE Trans Autom Control*. 1995;40(3):419-425.
52. Drincic B *Mechanical models of friction that exhibit hysteresis, stick-slip, and the stribeck effect* (Doctoral dissertation, University of Michigan); 2012.
53. Bouc R. Influence du cycle d'hysteresis sur la resonance non lineaire d'un circuit serie. In Colloq. Inter. du CNRS (Vol. 148, pp. 483–489);1964.
54. Bouc R. A mathematical model for hysteresis. *Acta Acust United Acust*. 1971;24(1):16-25.
55. Wen YK. Method for random vibration of hysteretic systems. *J Eng Mech Div*. 1976;102(2):249-263.
56. Wang CH, Wen Yk. *Reliability and redundancy of pre-Northridge low-rise steel buildings under seismic excitation*. na; 1998.
57. Song J, Der Kiureghian A. Generalized Bouc–Wen model for highly asymmetric hysteresis. *J Eng Mech*. 2006;132(6):610-618.
58. Aloisio A, Alaggio R, Köhler J, Fragiacomo M. Extension of generalized Bouc-Wen hysteresis modeling of wood joints and structural systems. *J Eng Mech*. 2020;146(3):04020001.
59. Dahl PR. A Solid Friction Model. Tech. Rep. Aerospace Corp El Segundo; 1968.
60. Mohammad Naser MF, Ikhouane F Consistency of the duhem model with hysteresis. *Math Probl Eng*. 2013;2013(586130). https://doi.org/10.1155/2013/586130
61. Visintin A. *Mathematical Models of Hysteresis*. In: Springer; 1996:71-80.
62. Baber TT, Wen YK. Random vibration of hysteretic, degrading systems. *J Eng Mech Div*. 1981;107(6):1069-1087.
63. Ismail M, Ikhouane F, Rodellar J. The hysteresis Bouc-Wen model, a survey. *Arch Comput Meth Eng*. 2009;16(2):161-188.
64. Pelliciari M, Marano GC, Cuoghi T, Briseghella B, Lavorato D, Tarantino AM. Parameter identification of degrading and pinched hysteretic systems using a modified Bouc–Wen model. *Struct Infrastruct Eng*. 2018;14(12):1573-1585.

65. Sirotti S, Pelliciari M, Di Trapani F, et al. Development and validation of new bouc–wen data-driven hysteresis model for masonry infilled rc frames. *J Eng Mech*. 2021;147(11):04021092.
66. De Santis Y, Fragiacomo M. Timber-to-timber and steel-to-timber screw connections: Derivation of the slip modulus via beam on elastic foundation model. *Eng Struct*. 2021;244:112798.
67. EN1995-1.1. 5-1. Eurocode 5: Design of timber structures–Part 1-1: General rules and rules for buildings. European Committee for Standardization (CEN); 2004.
68. Girhammar UA, Jacquier N, Källsner B. Stiffness model for inclined screws in shear-tension mode in timber-to-timber joints. *Eng Struct*. 2017;136:580-595.

SUPPORTING INFORMATION

Additional supporting information can be found online in the Supporting Information section at the end of this article.

How to cite this article: Boggian F, Aloisio A, Tomasi R. Experimental and analytical study of Friction Connection for seismic retrofit with Cross-Laminated Timber (CLT) panels. *Earthquake Engng Struct Dyn*. 2022;1-23. https://doi.org/10.1002/eqe.3724